Constant potential energetics of metallic and semiconducting electrodes: A benchmark study on 2D materials

Hedda Oschinski [iD] ; Nicolas Georg Hörmann [✉] [iD] ; Karsten Reuter [iD]

Check for updates

View Online

Export Citation

28 June 2024 08:41:02

The Journal of Chemical Physics

Special Topic:
Polaritonics for Next Generation Materials

Submit Today

AIP Publishing
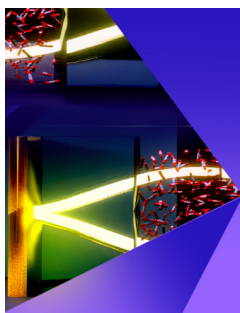
Constant potential energetics of metallic and semiconducting electrodes: A benchmark study on 2D materials

View Online   Export Citation   CrossMark

Hedda Oschinski,[1,2] (iD) Nicolas Georg Hörmann,[1,a)] (iD) and Karsten Reuter[1,2] (iD)

AFFILIATIONS

[1] Fritz-Haber-Institut der Max-Planck-Gesellschaft, Faradayweg 4-6, 14195 Berlin, Germany
[2] Technische Universität München, Lichtenbergstr. 4, 85747 Garching, Germany

[a)] Author to whom correspondence should be addressed: hoermann@fhi-berlin.mpg.de

ABSTRACT

Grand-canonical (GC) constant-potential methods within an implicit solvent environment provide a general approach to compute the potential-dependent energetics at electrified solid–liquid interfaces with first-principles density-functional theory. Here, we use a mindfully chosen set of 27 isostructural 2D metal halides MX_2 to analyze the variation of this energetics when the electronic structure changes from metallic to semiconducting and insulating state. Apart from expectable changes due to the opening up of the electronic bandgap, the calculations also show an increasing sensitivity to the numerical Brillouin zone integration and electronic smearing, which imposes computational burdens in practice. We rationalize these findings within the picture of the total interfacial capacitance arising from a series connection of the electrochemical double-layer capacitance and the so-called quantum capacitance resulting from the filling of electronic states inside the electrode. For metals, the electrochemical double-layer capacitance dominates at all potentials, and the entire potential drop takes place in the electrolyte. For semiconductors, the potential drop occurs instead fully or partially inside the electrode at potentials within or just outside the bandgap. For 2D semiconductors, the increased sensitivity to numerical parameters then results from the concomitantly increased contribution of the quantum capacitance that is harder to converge. Fortunately, this understanding motivates a simple extension of the CHE + DL approximation for metals, which provides the approximate GC energetics of 2D semiconductors using only quantities that can be obtained from computationally undemanding calculations at the point of zero charge and a generic double-layer capacitance.

I. INTRODUCTION

Semiconducting materials play an important role in various electrochemical applications.[1–3] Their existence in these applications may be deliberate as in photoelectrocatalysis or electrochemical growth[4–6] or unintentional as a result of metal surface oxidation or solvent decomposition.[7–9] Despite this relevance, first-principles modeling of extended electrified semiconductor–electrolyte interfaces is much less developed than for metal electrodes. Arguably, this is connected to the uncertain transferability of the prevalent approximate modeling approach for the latter in the form of the Computational Hydrogen Electrode (CHE).[10–12] Within a thermodynamic setup, the CHE efficiently captures the influence of an aqueous electrochemical environment (bias, pH) through the consideration of

appropriate reservoirs for electrons and protons. In most applications, the actual electronic structure of the electrode–electrolyte interface is treated at the point of zero charge (PZC).[13] While the latter enables computationally appealing electronic structure calculations of uncharged surface slabs in periodic boundary condition (PBC) supercells, the incurred neglect of electronic polarization at the electrochemical interface could be particularly questionable for semiconducting electrodes. As a result of the limited availability of electronic charge carriers,[14,15] the electronic surface structure of these electrodes is, after all, non-trivially modified by the capacitive charging of the interface upon electrification.[7]

The recent development of grand-canonical (GC) constant potential methods offers a direct and general route to the energetics of electrochemical interfaces under applied potential

conditions.[16–23] In particular, approximations such as the CHE + DL approach[20,23,24] allow for an account of capacitive charging at computational costs comparable to the CHE. Meanwhile, these methods have primarily been developed with metal electrodes in mind. In this article, we, therefore, assess the transferability and necessary adaptions for the application to 2D semiconductor electrodes. We thereby specifically aim to establish an analog of the computationally appealing CHE + DL approximation, and we focus particularly on layered "2D" materials. Apart from the intrinsic relevance of this class of materials,[25–28] the motivation for the latter focus comes from the fact that extended effects of the interfacial polarization like band bending inside the semiconductor material do not yet occur. At the same time, especially the family of isostructural 2D metal halides[29] spans metals, semiconductors, and insulators and constitutes, therefore, an ideal comparative testing ground for this transferability study without any disturbance due to structural changes.

Our calculations show that the potential dependence of the GC energetics at the semiconducting and insulating 2D halides is, indeed, fundamentally different from the one at the metallic halides. However, in line with existing phenomenological descriptions,[30–36] these differences are readily traced back to the influence of the material's electronic density-of-state (DOS) on the interfacial capacitance. This understanding then motivates a straightforward extension of the CHE + DL approximation, essentially simply by accounting for the size and position of the bandgap computed at the PZC. This maintains the computational appeal of only requiring calculations performed in charge-neutral supercells and provides a solid starting ground for future work that then additionally includes an extended space-charge layer formation in extended semiconductor electrodes of finite width.

II. METHODS

A. 2D metal halide model systems

We focus our calculations on a set of 27 isostructural (transition) metal halides of MX_2 structure in an aqueous environment. As illustrated in Fig. 1, these "2D" materials exhibit a trilayer geometry with hexagonal surface unit-cell (space group $P\bar{3}m1$). In a recent theoretical study, 26 of these halides were identified as easily exfoliable from their 3D parent materials.[29] TiI_2 was added manually to achieve a complete dataset with the three halides X = Br, Cl, I and nine metal atoms M = Mg, Ti, V, Mn, Fe, Co, Ni, Zn, Cd. Fifteen of these halides are metallic, and 12 are semiconducting or insulating with computed bandgaps spanning the entire range up to and
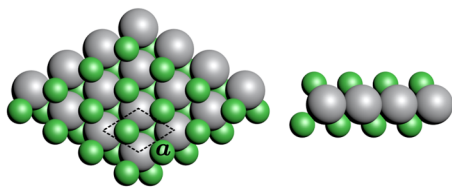
FIG. 1. Top and side views of the MX_2 metal halides considered in this study. Shown in dashed lines is the primitive hexagonal surface unit-cell with lattice parameter a. The halide atoms X are shown as smaller green spheres, and the metal atoms M are shown as larger gray spheres.

above 4 eV. Section S1 of the supplementary material lists all relevant material properties of the dataset, such as lattice constants, frontier level positions, and bandgaps, all of which show clear trends when varying for a given metal atom M the halide X, and equally when changing for a given halide X the metal atom M. In general, bandgaps increase and valence band positions decrease when going from I to Br to Cl. (See Sec. S1 of the supplementary material for more details.)

B. Computational details

All electronic structure theory calculations were performed at the density-functional theory (DFT) level using the plane wave and pseudopotential-based code Quantum ESPRESSO (QE)[37,38] and the AiiDA Quantum ESPRESSO workflow package.[39] Pseudopotentials were taken from the GBRV pseudopotential library (version 1.5)[40] with density and wavefunction cutoffs at `ecutwfc` = 45 Ry and `ecutrho` = 360 Ry, respectively. The electronic convergence threshold for self-consistency was set to 1.0×10^{-11} Ry, and Brillouin zone integrations used Γ-centered Monkhorst–Pack meshes and Gaussian smearing (see below). The electronic exchange and correlation is treated at the level of the semi-local PBE[41] functional. While PBE is known to underestimate bandgaps,[42] this quantitative deficiency does not matter for the present systematic trend study. Test calculations carried out with the dispersion-corrected meta-GGA rVV10[43] and hybrid HSE[44] functional show some quantitative changes, without affecting any of the methodological derivations or conclusions. A more detailed analysis on quantitative differences for $MgCl_2$ can be found in Sec. S2 A of the supplementary material.

The employed PBC supercell contains one MX_2 trilayer taken from the Materials Cloud database[29] and separated by 20 Å in the z-direction from its next periodic images. A (1×1) surface unit-cell was employed throughout, and no spin polarization was considered. We note that some of the materials show, in principle, either a ferromagnetic or an antiferromagnetic behavior.[29] For completeness, we assessed explicitly spin effects for three selected materials $FeCl_2$, FeI_2, and NiI_2. While $FeCl_2$ and NiI_2 converge to a ferromagnetic, metallic and a ferromagnetic, semimetallic groundstate, respectively, the electronic structure of FeI_2 remains unchanged when including two spin channels. In all cases, we find that spin polarization does not affect the central conclusions of this study (see Sec. S2 B of the supplementary material).

The uncharged MX_2 trilayer was fully relaxed at the optimized lateral PBE lattice constant a, cf. Fig. 1, until residual forces fell below 1.0×10^{-3} Ry/Bohr. Charged calculations were then performed in a single-point fashion at this frozen geometry.

The aqueous electrolyte was considered through an implicit solvation model.[13] Specifically, we employed the SCCS implementation in the ENVIRON module[38,45] with soft interface parameters set to `rhomax` = 0.005 and `rhomin` = 0.0001, and applying the nonlinear size-modified Poisson–Boltzmann equation. The temperature was set to 300 K with a molar concentration of the ionic counter charge of 1 mol l^{-1} and a valence of the ionic counter charge of ± 1. The solvent radius was fixed to 2.6 Å, and the filling threshold was fixed to 0.75 Å. The surface tension of the environment was set to 0 dyn/cm, and the external pressure of the environment was set to 0 GPa. For the static dielectric permittivity of the electrostatic continuum embedding model, we chose 78.3.

28 June 2024 08:41:02

The possibility to consider counter charges in the implicit electrolyte allows us to compute halide trilayers at varying amounts of excess electrons N_e while keeping the overall PBC supercell charge neutral.[13] The GC energy $\mathscr{E}(\tilde{\mu}_e)$ discussed below is related to the corresponding canonical constant-charge total energies $E(N_e)$ via a Legendre–Fenchel transform,

$$\mathscr{E}(\tilde{\mu}_e) = \min_{N_e} \{E(N_e) - N_e \tilde{\mu}_e(N_e)\}, \tag{1}$$

where e is the elementary charge and $\tilde{\mu}_e$ is the electron's electrochemical potential. Numerically, we evaluate this transform by computing the systems in a range of charge states spanning $-0.1e \leq N_e \cdot e \leq 0.1e$ in steps of $0.005\,e$. The electron's electrochemical potential in these computations is thereby given by the Fermi energy $\varepsilon_F(N_e)$ relative to the electrostatic potential in solution ϕ^S,

$$\tilde{\mu}_e(N_e) = -(\varepsilon_F(N_e) - e \cdot \phi^S), \tag{2}$$

where in QE + ENVIRON with included parabolic PBC correction $\phi^S = 0$ is set as zero reference.[46]

Previous studies[47,48] indicated the possibility of non-convex $E(N_e)$ relationships for semiconducting systems and possible problems to evaluate the Legendre transform as in Eq. (1) accurately in the bandgap region, where the Fermi level position is ill-defined at 0 K. However, we do not observe any such problems for any of the studied systems in the present work. Indeed, fundamental considerations suggest that $E(N_e)$ is piecewise linear at 0 K and becomes continuously differentiable and increasingly convex at finite temperature or with common smearing methods. Equally, systems with non-convex $E(N_e)$ relationships are expected to phase-separate in the large system size limit, e.g., by the condensation of an appropriate amount of polarons in order to fall back on the linear or convex ground state energetics. In summary, we believe that Eq. (1), and therewith implicitly $\frac{\partial E}{\partial N_e} = \tilde{\mu}_e$, holds in most cases, in particular for all systems studied in the present work (see, for example, our results in Sec. S3 of the supplementary material).

A standard quality (SQ) Brillouin zone sampling with a $(12 \times 12 \times 1)$ k-point grid and a Gaussian smearing width of $\sigma = 0.01$ Ry was found to be fully sufficient to perform geometry optimizations and achieve converged energetics. For the metallic halides, these SQ settings also converge the interfacial capacitance C, cf. definition below. In contrast, this is not the case for the halides with a bandgap, which are in a semiconducting state in the uncharged calculations and in a metallic state in the charged calculations. While the prior semiconducting state demands a smearing width reflecting room temperature, the latter conducting state then requires an excessive k-point sampling to converge the capacitance. In Sec. III, we demonstrate this by high quality (HQ) settings, which employ a $(84 \times 84 \times 1)$ k-point grid together with a room-temperature Gaussian smearing width of $\sigma = 0.002$ Ry. As detailed in the supplementary material (Figs. S47–S48), no further changes in the capacitance were then obtained when further increasing the k-point grid up to $(400 \times 400 \times 1)$. In addition, we find that Gaussian smearing leads essentially to identical results as Fermi–Dirac smearing (see subsequent discussions and Sec. S2 D of the supplementary material).

III. RESULTS AND DISCUSSION

A. General behavior of GC energies from metals to insulators

Within *ab initio* thermodynamics considerations, differences of GC energies of different system states typically appear with additional chemical potential terms (reflecting thermodynamic reservoirs) of, for example, protons balancing any differences in corresponding species between the involved system states.[13] The central differences between metallic and semiconducting 2D electrodes lie only in the distinct dependence on the electron electrochemical potential $\tilde{\mu}_e$. As a result, we concentrate in the following on $\mathscr{E}(\tilde{\mu}_e)$ to generally discuss possible differences in the fundamental behavior of the GC energetics at metal and semiconductor 2D electrodes, and a concomitant adaption of the computationally appealing CHE + DL approximation. For metallic electrodes, the applied electrode potential Φ_E is directly related to the electron's electrochemical potential in the bulk electrode $\tilde{\mu}_e = -e\Phi_E$ such that the GC energy $\mathscr{E}(\tilde{\mu}_e)$ can be directly reexpressed as a function of the applied electrode potential Φ_E. This direct relation does not necessarily hold for extended semiconductors;[48] nonetheless, assessment of the grand canonical energy as a function of $\tilde{\mu}_e$ as in Eq. (1) remains meaningful in general, as long as $E(N_e)$ is convex, which holds for all studied 2D systems in the present work. Our present analysis corresponds thus to what is referred to as constant Fermi level energetics in Ref. 48 but not to the constant inner potential (CIP) energetics, whose application to 2D materials remains unclear due to a missing bulk-like inner potential region.

Figure 2 displays the computed $\mathscr{E}(\tilde{\mu}_e)$ for three metal chlorides, TiCl$_2$, FeCl$_2$, and MgCl$_2$. This selected group contains one metal (TiCl$_2$), one semiconductor with a computed gap of 0.9 eV (FeCl$_2$), and one insulator with a computed gap of 6.0 eV (MgCl$_2$),
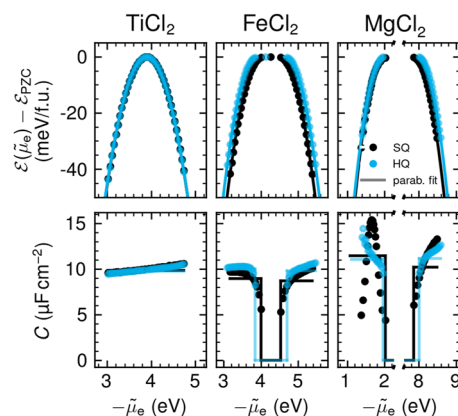
FIG. 2. Top panels: GC energy $\mathscr{E}(\tilde{\mu}_e)$ as a function of the electron's electrochemical potential $\tilde{\mu}_e$ and relative to the point of zero charge (PZC) for the three metal chlorides, TiCl$_2$ (no bandgap), FeCl$_2$ (small bandgap), and MgCl$_2$ (large bandgap). Shown are computed data for a Brillouin zone sampling at standard quality (SQ, black) and high quality (HQ, blue), see the text, together with a corresponding parabolic fit to the respective data (black and blue solid lines). Bottom panels: Interfacial capacitance C for the three chlorides as obtained numerically (dots) and through the second derivative of the fitted parabolas (solid line). Shown are again data at both levels of Brillouin zone sampling (black and blue).

which thus allows us to concisely discuss trends. As shown in the supplementary material, all remaining 24 MX$_2$ metal halides, indeed, exhibit a behavior that is fully consistent with the insights derived here on the basis of this showcase group. The potential dependence of $\mathscr{E}(\tilde{\mu}_e)$ is qualitatively different in the three cases. While the metallic TiCl$_2$ exhibits a seemingly parabolic behavior around the PZC, the two branches of the parabola for positive and negative potentials are separated for the other two chlorides, with a separation that matches their bandgap, similarly to what was already described for TiO$_2$.[48]

Quantitatively, the potential dependencies are, in fact, also not exactly parabolic. This is better visible by plotting the area-normalized interfacial capacitance $C(\tilde{\mu}_e)$ as the formal second derivative of the GC energy with respect to the electron's electrochemical potential, see below. Figure 2 compares the numerically computed data with the analytical second derivative of a parabolic fit to the GC energies. While the numerically computed $C(\tilde{\mu}_e)$ is, indeed, essentially constant over the tested potential range in the case of the metallic TiCl$_2$, it does not at all show an at least piecewise constant profile for the other two chlorides as would be expected for the case of a split parabola. Moreover, in the latter two cases, there is also an increasing sensitivity to the accuracy of the Brillouin zone sampling performed in the DFT calculations. For the small bandgap FeCl$_2$, there are already notable differences between a standard quality and a high quality sampling; see Sec. II B. For the large bandgap MgCl$_2$, the behavior at the lower SQ settings is then completely unconverged. We verified that the HQ settings correspond to full convergence in all three cases.

B. Decomposing the interfacial capacitance

In order to gain further insights into the different potential dependencies and sensitivities to Brillouin zone sampling, we start by explicitly considering the relation between the GC energy and the area-normalized interfacial capacitance. Relative to the situation at the PZC with $\tilde{\mu}_e^0 = \tilde{\mu}_e(0)$, this is

$$\mathscr{E}(\tilde{\mu}_e) = \mathscr{E}_{PZC}(\tilde{\mu}_e^0) - \frac{A}{e^2} \int_{\tilde{\mu}_e^0}^{\tilde{\mu}_e} \int_{\tilde{\mu}_e^0}^{\tilde{\mu}_e'} C(\tilde{\mu}_e') \, d\tilde{\mu}_e' \, d\tilde{\mu}_e, \qquad (3)$$

with A being the interfacial area. For an approximately constant interfacial capacitance over the studied potential range, $C(\tilde{\mu}_e) \sim C_0$ = const., this straightforwardly yields a parabolic form

$$\mathscr{E}(\tilde{\mu}_e) \approx \mathscr{E}_{PZC}(\tilde{\mu}_e^0) - \frac{AC_0}{2e^2} (\tilde{\mu}_e^0 - \tilde{\mu}_e)^2. \qquad (4)$$

In fact, with C_0 being the interfacial capacitance at the PZC, this is exactly the CHE + DL energy expression with a phenomenological quadratic potential dependence[20,24,49] used before for metal electrodes.

However, as obvious from Fig. 2, the underlying assumption of an essentially constant interfacial capacitance does not hold for systems with a bandgap. For the latter systems, the potential dependence of $C(\tilde{\mu}_e)$ needs to be explicitly considered. To further analyze this dependence, we rewrite the definition of $C(\tilde{\mu}_e)$ through Eq. (3) using Eq. (1),

$$
\begin{aligned}
C(\tilde{\mu}_e) &= \frac{e^2}{A} \left(\frac{\partial^2 \mathscr{E}(\tilde{\mu}_e)}{\partial \tilde{\mu}_e^2} \bigg|_{\tilde{\mu}_e} \right) \\
&= \frac{e^2}{A} \left(\frac{\partial N_e(\tilde{\mu}_e)}{\partial \tilde{\mu}_e} \bigg|_{\tilde{\mu}_e} \right) \\
&= \frac{e^2}{A} \left(\frac{\partial \tilde{\mu}_e(N_e)}{\partial N_e} \bigg|_{N_e(\tilde{\mu}_e)} \right)^{-1},
\end{aligned}
\qquad (5)
$$

which can be evaluated if the respective functions are continuously differentiable (e.g., for $T > 0$ K or with employed smearing). By introducing a material-intrinsic electrostatic reference ϕ^I, we can rewrite Eq. (2) as

$$\tilde{\mu}_e(N_e) = \underbrace{-\left(\varepsilon_F(N_e) - e\phi^I(N_e)\right)}_{\mu_e} + \underbrace{\left(-e(\phi^I(N_e) - \phi^S)\right)}_{-e\phi^{eDL}}, \qquad (6)$$

which phenomenologically introduces a decomposition of the electron electrochemical potential into chemical and electrostatic parts. The chemical contribution μ_e is hereby given by the Fermi level position relative to the inner reference potential ϕ^I and the electrostatic part by the relative shift of ϕ^I relative to the bulk solution reference ϕ^S. In general, a decomposition into chemical and electrostatic parts remains ambiguous as any material-intrinsic potential reference ϕ^I is only defined up to a constant that equally applies to the terms *inner potential* or *Galvani potential*, frequently used in electrochemistry. Gratifyingly, $C(\tilde{\mu}_e)$ remains unaffected by such constant offsets and, as a result, can be written as

$$
\begin{aligned}
C^{-1}(\tilde{\mu}_e) &= \frac{A}{e^2} \left(\frac{\partial \mu_e}{\partial N_e} \bigg|_{N_e(\tilde{\mu}_e)} + \frac{-e\partial \phi^{eDL}}{\partial N_e} \bigg|_{N_e(\tilde{\mu}_e)} \right) \\
&= C_{DOS}^{-1}(\tilde{\mu}_e) + C_{eDL}^{-1}(\tilde{\mu}_e).
\end{aligned}
\qquad (7)
$$

This leads thus to the well-established picture of the total interfacial capacitance in terms of a series connection of the capacitance of the electrode and the capacitance of the electrochemical double layer (eDL). The first contribution, the DOS capacitance (sometimes also called the quantum capacitance) with

$$C_{DOS}(\tilde{\mu}_e) = \frac{e^2}{A} D_\sigma(\varepsilon_F(\tilde{\mu}_e)), \qquad (8)$$

arises from the Fermi level shift relative to an inner potential reference ϕ^I as induced by the filling of the broadened electronic density of states,[50]

$$D_\sigma(\varepsilon_F) = \frac{\partial N_e}{\partial \mu_e} \bigg|_{\varepsilon_F}. \qquad (9)$$

DOS broadenings are intrinsically introduced when allowing non-integer occupations for electronic states, which is necessary for numerical reasons to obtain converged energetics and forces for metals or metalized semiconductors at finite k-point resolution.[51–54] In principle, realistic temperature-related broadening effects are obtained when Fermi–Dirac occupations are used in
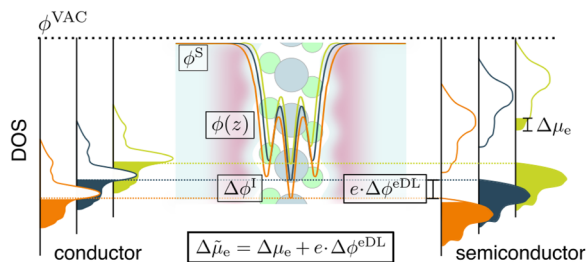
FIG. 3. Schematic representation of the DOS for a conducting and a semiconducting material and the average electrostatic potential in the z-direction $\phi(z)$ for a positive (orange) and a negative (green) charged state compared to the potential of zero charge (blue). It illustrates the shift of the electrochemical potential of an electron $\Delta\tilde{\mu}_e$—as a combination of the electrostatic shift of the whole DOS relative to the solution level ϕ^S by $e\Delta(\phi^I - \phi^S) = e\Delta\phi^{eDL}$ and the "chemical contribution" $\Delta\mu_e$—the shift of the Fermi level relative to an inner potential reference ϕ^I. The electrostatic potential converges to ϕ^S in the bulk solvent region, which can be referenced to the electrostatic potential in vacuum ϕ^{VAC}.

combination with a room temperature smearing width $\sigma = k_B T \sim 25$ meV.[50] However, it is common practice to use other occupation functions that can exhibit smaller artifacts at larger-than-room-temperature smearings at the expense of introducing unphysical electronic entropy contributions or non-unique Fermi levels.[51,52,54] For all practical purposes, the here used Gaussian smearing method yields equivalent results to Fermi–Dirac smearing for appropriately rescaled σ values (cf. Figs. S16 and S17 of the supplementary material), as demonstrated in Ref. 54. Nonetheless, the DOS capacitance is affected by electronic smearing via Eq. (8), which will be discussed below.

The double-layer capacitance,

$$C_{eDL}(\tilde{\mu}_e) = \frac{-e}{A} \frac{\partial N_e}{\partial \phi^{eDL}}\bigg|_{N_e(\tilde{\mu}_e)}, \qquad (10)$$

in turn derives from the electrostatic potential drop ϕ^{eDL} across the electrode–electrolyte interface as illustrated in Fig. 3.

While a more formal partitioning of $C(\tilde{\mu}_e)$ has been achieved by Binninger,[50] the more heuristic partitioning as in the present work is commonly applied in the assessment of low-dimensional electrodes, e.g., graphene,[30,31] MoS$_2$,[32] or carbon nanotubes,[33–35] and as we will see, the ensuing separate analysis of the two contributions $C_{DOS}(\tilde{\mu}_e)$ and $C_{eDL}(\tilde{\mu}_e)$ will bring very intuitive access to the different behavior of metallic and semiconducting electrodes.

1. The double-layer capacitance C$_{eDL}$

As elaborated before, the double-layer capacitance $C_{eDL}(\tilde{\mu}_e)$ can be evaluated by analyzing the shift of a material-intrinsic potential reference $\phi^I(N_e(\tilde{\mu}_e))$ relative to the solution reference ϕ^S. Common intuitive inner potential references established in the field of semiconductor band alignment[55] are the electrostatic potential at a point in the material (e.g., the center of the material), the average over the electrostatic potential inside the material, or the alignment of a characteristic state of the DOS, e.g., the conduction or valence band edge or a deep electronic (core-level) state.[30,56–60] While all these schemes should be equivalent for macroscopic electrodes,[61] we

found especially a spatial average of the electrostatic potential within the 2D material

$$\phi^I(N_e) = \frac{\int_{z_1}^{z_2} \phi(N_e, z)\,dz}{\int_{z_1}^{z_2} dz} \qquad (11)$$

to lead to robust numerical results in the present study (see Sec. S4 A of the supplementary material for comparison and discussion of the effects of different choices of electrostatic referencing). In this case, the finite difference estimate for C_{eDL}, cf. Eq. (10), is evaluated as

$$C_{eDL}(\tilde{\mu}_e) \approx -\frac{e}{A} \frac{\Delta N_e}{\Delta\phi^I}\bigg|_{N_e(\tilde{\mu}_e)}. \qquad (12)$$

Figure 4 shows the obtained $C_{eDL}(\tilde{\mu}_e)$ contribution for the three showcase metal chlorides. We obtain essentially no or only a very weak dependence on the Brillouin sampling and Gaussian smearing widths σ, and in the case of the metallic TiCl$_2$ and small bandgap semiconductor FeCl$_2$ also, there is only a negligible variation of $C_{eDL}(\tilde{\mu}_e)$ over the entire potential range. In contrast, the large bandgap insulator MgCl$_2$ shows a pronounced increase in C_{eDL} in the negative charging regime (similarly observed also for MgBr$_2$), which is enhanced by using the HSE functional. We attribute this anomalous behavior of $C_{eDL}(\tilde{\mu}_e)$ to the observed differences in the electronic excess charge distributions for these materials under these conditions, which is likely related to the large bandgap and/or the low electronic stability/work function of $-\tilde{\mu}_e \lesssim 2$ eV (cf. Secs. S2 A and S4 C of the supplementary material).

For all other halides with their smaller bandgaps (cf. Sec. S4 C of the supplementary material), the variations of $C_{eDL}(\tilde{\mu}_e)$ with charge state are within a minimal 2 μF cm^{-2} and there is no significant dependence on the Brillouin zone sampling and smearing. Moreover, there are also only minor variations of $C_{eDL}(\tilde{\mu}_e)$ over the studied set of metal halides. We can conclude that the capacitance contribution of the electrochemical double layer is an essentially material-independent constant with a value of about $C_{eDL}(\tilde{\mu}_e)$ ~ 10 μF cm^{-2} within the presently employed implicit solvation model.
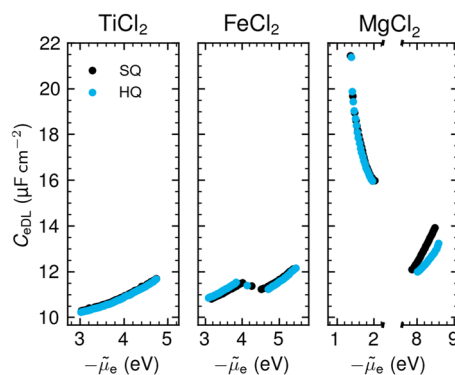
FIG. 4. Electrochemical double-layer capacitance C_{eDL} as a function of the electron's electrochemical potential $\tilde{\mu}_e$ and relative to the point of zero charge (PZC) for the three metal chlorides, TiCl$_2$ (no bandgap), FeCl$_2$ (small bandgap), and MgCl$_2$ (large bandgap). The results are again shown for a Brillouin zone sampling at standard quality (SQ, black) and high quality (HQ, blue).

2. The DOS capacitance C_{DOS}

The relative robustness of $C_{eDL}(\tilde{\mu}_e)$ is in stark contrast to the sensitivity observed for the DOS capacitance $C_{DOS}(\tilde{\mu}_e)$ in Fig. 5.

In order to be consistent with the finite difference evaluation of $C(\tilde{\mu}_e)$ and $C_{eDL}(\tilde{\mu}_e)$, we here also evaluate this contribution numerically by computing at each charge state the differential change of the Fermi level position $\Delta\varepsilon_F$ due to charging. In practice, we determine $\Delta\varepsilon_F$ consistent with the QE-internal routines using a bisection method to find ε_F for a given target total number of electrons, where $N_e(\varepsilon)$ is given within the employed Gaussian smearing method by

$$N_e(\varepsilon) = \sum_{k,b} w_k \cdot \frac{1}{2} \, \mathrm{erfc}\left(\frac{\varepsilon_{k,b} - \varepsilon}{\sigma} \right), \tag{13}$$

with w_k being the k-point weight, σ being the smearing width, and $\varepsilon_{k,b}$ being the energy of the Kohn–Sham eigenstate for k-point k and band b. This allows us to compute explicitly a finite-difference, broadened DOS consistent with the employed Gaussian smearing method,

$$D_\sigma(\varepsilon) \approx \frac{\Delta N_e(\varepsilon)}{\Delta\varepsilon}. \tag{14}$$

It thereby makes essentially no difference to use self-consistently determined Kohn–Sham energies $\varepsilon_{k,b}$ at each according charge state or to use $\varepsilon_{k,b}$ computed for the charge neutral system throughout. The effect of orbital relaxation on the DOS and DOS capacitance is negligible, as we show in Figs. S39 and S40 of the supplementary material. Finally, we also validated that the finite difference value $D_\sigma(\varepsilon_F(\tilde{\mu}_e))$ agrees with directly computed, temperature broadened DOS at HQ settings; cf. Figs. S14 and S15 of the supplementary material.

As apparent from Fig. 5, the $C_{DOS}(\tilde{\mu}_e)$ capacitance contribution varies largely over the studied range of potentials and requires a most accurate Brillouin sampling and small smearing width for convergence. The effect of the latter can be rationalized from additional free energy contributions $E_\sigma = -\sigma S(\sigma)$ introduced by smearing,[54] which affects the electron chemical potential (see Sec. S2 D of the supplementary material) approximately via

FIG. 5. Same as Fig. 4, but for the DOS capacitance C_{DOS}.

$$\mu_e \approx \mu_{e,0} + \frac{\partial}{\partial N_e}\left(-\sigma S(\sigma) \right) \tag{15}$$

$$= \mu_{e,0} + \frac{\partial E_\sigma}{\partial N_e}. \tag{16}$$

$\mu_{e,0}$ signifies hereby the chemical potential at nominally vanishing smearing, while the second term $\frac{\partial E_\sigma}{\partial N_e}$ introduces a σ-dependent shift. The latter term affects the charge-vs-chemical-potential relation as well as the DOS capacitance, e.g., whenever $\frac{\partial^2 E_\sigma}{\partial N_e^2} \neq 0$. An according detailed analysis of smearing contributions within our HQ vs SQ simulations can be found in Sec. S5 C of the supplementary material, which underlines the importance of realistically small smearing widths for semiconducting systems and their relative unimportance for the metallic systems. Most notably, the analysis can explain the observed closing-of-the-bandgap in the SQ settings (cf. Fig. 2) due to the altered charge-vs-chemical-potential relation via $\frac{\partial E_\sigma}{\partial N_e}$ (see Sec. S5 C of the supplementary material for more details).

For the converged HQ parameter set, $C_{DOS}(\tilde{\mu}_e)$ values obtained for the three metal chlorides differ widely and not surprisingly $C_{DOS}(\tilde{\mu}_e) = 0$ within the potential range corresponding to the bandgap of $FeCl_2$ and $MgCl_2$. These distinct changes in magnitude thereby nicely rationalize the differing behavior of the GC energetics and total interfacial capacitance observed originally in Fig. 2. In case of the metallic $TiCl_2$, the $C_{DOS}(\tilde{\mu}_e)$ contribution is always orders of magnitude larger than the $C_{eDL}(\tilde{\mu}_e)$ contribution. In the capacitor series connection, it, therefore, plays no role for the total interfacial capacitance, and $C(\tilde{\mu}_e)$ is completely determined by the essentially constant electrochemical double-layer capacitance that is furthermore already converged at undemanding Brillouin sampling settings. This large $C_{DOS}(\tilde{\mu}_e)$ across the full potential range, therefore, justifies the constant capacitance assumption of the conventional CHE + DL approximation and a simple parabolic potential dependence of the GC energetics results. We emphasize that the particularly small variation of $C_{eDL}(\tilde{\mu}_e)$ is a direct consequence of the employed implicit solvation model.[13,62,63] While explicit solvation models lead to somewhat larger variations at very high electrolyte concentrations,[64] the CHE + DL approximation remains useful for understanding the experimentally relevant regime of intermediate and low electrolyte concentrations.

The situation becomes a bit more complex for the two cases with a bandgap. Here, $C_{DOS}(\tilde{\mu}_e) = 0$ within the bandgap. This will then always dominate the total capacitance and necessarily delay any potential variation of $\mathcal{E}^{DFT}(\tilde{\mu}_e)$ to potentials outside of this range. This rationalizes the separation of the two branches of the parabola in Fig. 2 for $FeCl_2$ and $MgCl_2$. With $C_{DOS}(\tilde{\mu}_e)$ rising to finite values for potentials above or below the bandgap, it will initially exhibit similar magnitudes as $C_{eDL}(\tilde{\mu}_e)$. The total capacitance then receives significant contributions from both capacitances and will consequently exhibit the $C_{DOS}(\tilde{\mu}_e)$-induced sensitivity to the Brillouin sampling and smearing and a more complex potential dependence imposed by the non-constancy of $C_{DOS}(\tilde{\mu}_e)$. The potential range over which $C(\tilde{\mu}_e)$ shows this behavior depends on how quickly and if at all $C_{DOS}(\tilde{\mu}_e)$ will take on values that are much larger than $C_{eDL}(\tilde{\mu}_e)$. Once this happens, we are back to the situation seen for the metallic $TiCl_2$, with a parabolic GC energy variation resulting from the then again dominant constant $C_{eDL}(\tilde{\mu}_e)$. As seen in Fig. 2, this happens over a relatively small potential range
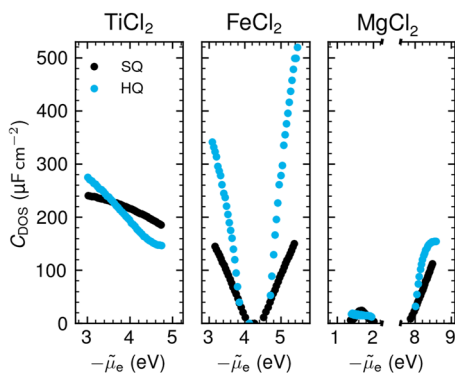
for FeCl$_2$, whereas in the case of MgCl$_2$, the two capacitance contributions remain of comparable magnitude for a larger range of potentials, especially within the SQ settings. The pronounced difference between the SQ and HQ behaviors thereby elucidates that the initial slower increase in C_{DOS} is mainly a smearing effect, whereas the later decrease in C_{DOS} in the negative charge range is a consequence of the poorly sampled k-point grid (cf. Fig. S15 of the supplementary material). A detailed display for the other materials can be found in the supplementary material (Sec. S5). Furthermore, the symmetry of the DOS around the bandgap and, correspondingly, the symmetry of $C_{DOS}(\tilde{\mu}_e)$ largely vary. While for FeCl$_2$, we find a rather symmetric behavior, similar to graphene,[30,65] $C_{DOS}(\tilde{\mu}_e)$ is asymmetric for MgCl$_2$. These trends can be directly mapped to the form of the DOS of both materials (cf. Sec. S5 of the supplementary material). Even though asymmetries can be observed also for some other materials, we will show in Sec. III C that such details can be neglected when considering the energetics.

C. CHE + DL approximation for 2D semiconductors

Even though the preceding analysis revealed a potential dependence of $C(\tilde{\mu}_e)$ for the 2D semiconductors that is generally more complex than a piecewise constant behavior, we recall that the assumption of a constant C_0 in the CHE + DL approximation for metals is also not strictly fulfilled. Nevertheless, the CHE + DL approximation has proven quite accurate in a number of cases.[20,23,24] In this spirit, the primary modification required for a CHE + DL application to gapped systems would be to replace the constant capacitance assumption with a piecewise constant capacitance assumption. Such a potential dependence of $C(\tilde{\mu}_e)$ would result if $C_{DOS}(\tilde{\mu}_e)$ switched in a stepwise fashion from 0 to a very large value at the valence band edge and the conduction band edge potentials. Outside of the bandgap potentials, the total capacitance is then given by $C_{eDL}(\tilde{\mu}_e)$, which is approximated by a constant value C_{eDL} that is furthermore primarily given by the solvation model.

Translated to the GC energetics, this generalization of the CHE + DL approximation then takes the following form:

$$\mathscr{E}^{CHE+DL}(\tilde{\mu}_e)$$

$$= \mathscr{E}_{PZC}(\tilde{\mu}_e) - \begin{cases} \dfrac{AC_{eDL}}{2e^2}\left(\tilde{\mu}_e^{cbe} - \tilde{\mu}_e\right)^2 & \text{if } \tilde{\mu}_e > \tilde{\mu}_e^{cbe}, \\ 0 & \text{if } \tilde{\mu}_e^{cbe} > \tilde{\mu}_e > \tilde{\mu}_e^{vbe}, \\ \dfrac{AC_{eDL}}{2e^2}\left(\tilde{\mu}_e^{vbe} - \tilde{\mu}_e\right)^2 & \text{if } \tilde{\mu}_e < \tilde{\mu}_e^{vbe}, \end{cases}$$

(17)

with two parabolic branches defined by C_{eDL} and the positions of valence and conduction band edges at the PZC $\tilde{\mu}_e^{vbe/cbe}$. Note that in the case of a vanishing bandgap, this expression reduces to the established CHE + DL approximation for metals if one identifies $C_{eDL} = C_0$. With $\tilde{\mu}_e^{vbe/cbe}$, the expression also primarily depends again on quantities that can accessibly be calculated in uncharged supercells and at standard Brillouin zone sampling. As C_{eDL} is not strongly material dependent, a generic value for the employed solvation model may be used for this remaining parameter. In Fig. 6, the performance of this extended CHE + DL approximation is correspondingly evaluated for the three showcase chlorides and simply using the generic value $C_{eDL} = 10 \ \mu F \ cm^{-2}$ derived above for the
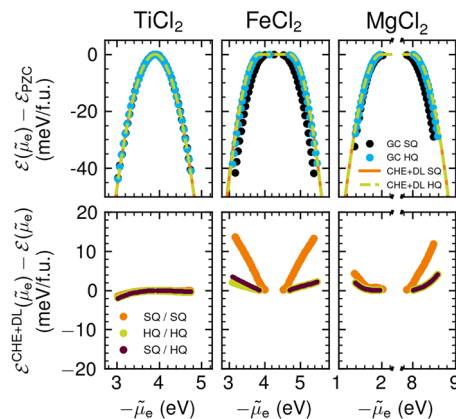
FIG. 6. Accuracy of the extended CHE + DL approximation for metals and gapped system for the three metal chlorides, TiCl$_2$ (no bandgap), FeCl$_2$ (small bandgap), and MgCl$_2$ (large bandgap). Top panels: Comparison of the GC energy $\mathscr{E}(\tilde{\mu}_e)$ as a function of the electron's electrochemical potential $\tilde{\mu}_e$ and relative to the point of zero charge (PZC) (dots) with the CHE + DL approximation $\mathscr{E}^{CHE+DL}(\tilde{\mu}_e)$ and using the generic value $C_{eDL} = 10 \ \mu F \ cm^{-2}$ (solid line). Bottom panels: Energy difference $\mathscr{E}^{CHE+DL}(\tilde{\mu}_e) - \mathscr{E}(\tilde{\mu}_e)$. The energetic accuracy of the CHE + DL model across the whole dataset is consistently within 7 meV/f.u. when compared to the HQ reference results. All panels show data computed at standard quality (SQ, black) and high quality (HQ, blue) Brillouin zone sampling.

present solvation model. For metal, semiconductor, and insulator, the energetic accuracy is consistently within 7 meV/f.u. when compared to the HQ reference results. As detailed in Figs. S47 and S48 of the supplementary material, a similar accuracy is obtained for all other halides, which should be perfectly sufficient for standard applications. As our benchmark study on 27 materials reveals the negligible importance of orbital relaxation effects under charged conditions (cf. Figs. S39 and S40 of the supplementary material), it is straightforward to extend the model even to cases with pronounced capacitance asymmetry, e.g., by considering more explicitly DOS capacitance contributions from PZC calculations.

IV. SUMMARY AND CONCLUSION

Computing the potential-dependent GC energetics for a mindfully chosen test set of 2D (transition) metal halides, we obtained fundamental differences between metallic and semiconducting systems. These differences involved not only the expectable effect of the opening bandgap but also an increasing sensitivity to the numerical Brillouin zone sampling and smearing width. Even though the results thus confirm the transferability of the recently introduced GC constant-potential (Fermi level) methodology to 2D semiconductors, achieving converged such calculations will, therefore, become a computational burden in practice. This provides further motivation to establish an extension of the computationally efficient CHE + DL approximation.

Our analysis traced the different behavior of gapped systems back to an increased contribution of the DOS capacitance of the electrode to the total interfacial capacitance. In the case of metals, the latter capacitance is dominated by the contribution from

the electrochemical double layer, which does not require particular care in terms of Brillouin zone sampling or smearing width to converge. Moreover, this quantity was not found to be particularly material specific across the studied set of 2D halides and is well approximated by a constant $C_{eDL} = 10$ μF cm^{-2} for the here employed implicit solvation model for the aqueous environment. For 2D semiconductors, it is, instead, the DOS capacitance contribution that introduces a more complex potential dependence and thus requires high Brillouin zone sampling accuracy and realistically small smearing widths.

This understanding then motivates a straightforward and simple extension of the CHE + DL approximation. In the spirit of this approximation for metals, this extension considers a piecewise constant interfacial capacitance, with zero value for Fermi level positions within the bandgap range and a finite value C_{eDL} at Fermi level positions outside. Despite this simplicity, the extension was found to show a reasonable accuracy across the entire halide test set. It also only requires input quantities that can be computed in charge neutral supercells and at undemanding Brillouin zone sampling settings, which thus preserves the computational appeal of the CHE + DL approximation for metals.

On a broader scope, the understanding that motivates this CHE + DL approximation aligns closely with the semi-classical picture for extended semiconductors at applied potentials that lie within the bandgap. In this case, similarly as here, application of an electrode potential does not directly translate into an electrostatic potential drop in the solution, as a dominant part of the applied potential drops inside the electrode due to the buildup of a macroscopic space-charge layer. As a corollary, this suggests that a simple augmentation of adsorption energies obtained under PZC conditions with dipole-field interactions—as valid for metallic systems due to the generic single-parabola-energetics[20,66,67]—might break down here, as was also put forward by Dominguez and Melander.[68] This is supported by recent constant inner potential calculations at semiconducting electrodes,[48] which equally suggest that their understanding and accurate, *ab initio*-based description is still in its infancy.[48] However, we anticipate that an analysis route analogous to the one pursued here based on a generic energy expansion may help us understand better the constant inner potential methodology, the energetics, and therewith the electrochemical behavior of extended semiconductor electrodes in the future.

SUPPLEMENTARY MATERIAL

The supplementary file contains the following: Table S1/Fig. S1: Lattice parameter for all studied structures. Figure S2: Valence and conduction band edges for all materials. Figure S3: Bandgaps for all materials. Figure S4: Valence band edge/Fermi level for all materials. Figure S5: Influence of the DFT functional on DFT energy, electron electrochemical potential, and differential capacitance of $MgCl_2$. Figure S6: Influence of the DFT functional on the DOS of $MgCl_2$. Figure S7: Influence of the DFT functional on the double-layer capacitance of $MgCl_2$. Figure S8: Influence of the DFT functional on the electrostatic potential of $MgCl_2$. Figure S9: Comparison of HSE and PBE regarding the excess electron density and the onset of the dielectric permittivity of $MgCl_2$. Figure S10: Influence of spin-polarization on the electron electrochemical potential and the DOS of $FeCl_2$, FeI_2, and NiI_2. Figure S11: Influence of spin-polarization on the capacitances with the CHE + DL approximated energetics of $FeCl_2$, FeI_2, and NiI_2. Figure S12: K-point and Gaussian smearing convergence for $TiCl_2$, $FeCl_2$, and $MgCl_2$. Figure S13: K-point and Gaussian smearing influence on the DOS for $TiCl_2$, $FeCl_2$, and $MgCl_2$. Figure S14: NSCF results and analytical DOS for $TiCl_2$, $FeCl_2$, and $MgCl_2$. Figure S15: Close view of Fig. S14 for $MgCl_2$. Figure S16: Comparison of Gaussian and Fermi–Dirac smearing regarding DFT energy, electron electrochemical potential, and DOS of $TiCl_2$, $FeCl_2$, and $MgCl_2$. Figure S17: Comparison of Gaussian and Fermi–Dirac smearing regarding the capacitances with the CHE + DL approximated energetics of $TiCl_2$, $FeCl_2$, and $MgCl_2$. Figures S18 and S19: DFT energies with respect to the cell charge for all materials. Figures S20 and S21: Electron electrochemical potential with respect to the cell charge for all materials. Figures S22 and S23: Differential capacitance with respect to the cell charge for all materials. Figure S24: Mean capacitance for all materials. Figure S25: Mean capacitance in the negative/positive charge range for all materials. Figure S26: Double-layer capacitance as determined with three different approaches vs differential capacitance for all materials. Figures S27 to S30: Electrostatic potential difference for the SQ and HQ parameters for all materials. Figure S31: Mean double-layer capacitance for all materials. Figure S32: Mean double-layer capacitance in the negative/positive charge range for all materials. Figures S33 and S34: Double-layer capacitance with respect to the cell charge for all materials. Figure S35: Influence of the halide atom regarding the excess electron density and the onset of the dielectric permittivity of TiX_2, FeX_2, and MgX_2. Figure S36: Comparison of $FeCl_2$ and $MgCl_2$ regarding the excess electron density and the onset of the dielectric permittivity. Figure S37: Mean DOS capacitance for all materials. Figure S38: Mean DOS capacitance in the negative/positive charge range for all materials. Figures S39 and S40: DOS capacitance with respect to the cell charge for all materials. Figures S41 and S42: DOS for all materials. Figures S43 and S44: Derivative of the smearing energy for all materials. Figures S45 and S46: Relative smearing error of the DOS capacitance for all materials. Figures S47 and S48: Comparison of the GC energy with the CHE + DL approximation for all materials.

AUTHOR DECLARATIONS

Conflict of Interest

The authors have no conflicts to disclose.

Author Contributions

Hedda Oschinski: Conceptualization (equal); Data curation (equal); Formal analysis (equal); Investigation (equal); Methodology (equal);

28 June 2024 08:41:02

DATA AVAILABILITY

The data that support the findings of this study are available from the corresponding author upon reasonable request.

REFERENCES

[1] H. Gerischer, "The impact of semiconductors on the concepts of electrochemistry," Electrochim. Acta **35**, 1677–1699 (1990).

[2] A. Eftekhari, "Molybdenum diselenide ($MoSe_2$) for energy storage, catalysis, and optoelectronics," Appl. Mater. Today **8**, 1–17 (2017).

[3] I. Dharmadasa, P. A. Bingham, O. Echendu, H. Salim, T. Druffel, R. Dharmadasa, G. Sumanasekera, R. Dharmasena, M. Dergacheva, K. Mit et al., "Fabrication of CdS/CdTe-based thin film solar cells using an electrochemical technique," Coatings **4**, 380–415 (2014).

[4] L. Kavan, M. Grätzel, S. Gilbert, C. Klemenz, and H. Scheel, "Electrochemical and photoelectrochemical investigation of single-crystal anatase," J. Am. Chem. Soc. **118**, 6716–6723 (1996).

[5] D. Merki, S. Fierro, H. Vrubel, and X. Hu, "Amorphous molybdenum sulfide films as catalysts for electrochemical hydrogen production in water," Chem. Sci. **2**, 1262–1267 (2011).

[6] S. M. Ahmed and H. Gerischer, "Influence of crystal surface orientation on redox reactions at semiconducting MoS_2," Electrochim. Acta **24**, 705–711 (1979).

[7] W. Schmickler and E. Santos, Interfacial Electrochemistry, 2nd ed. (Springer Science and Business Media, Berlin, Heidelberg, 2010).

[8] M. Grdeń, M. Łukaszewski, G. Jerkiewicz, and A. Czerwiński, "Electrochemical behaviour of palladium electrode: Oxidation, electrodissolution and ionic adsorption," Electrochim. Acta **53**, 7583–7598 (2008).

[9] A. Wang, S. Kadam, H. Li, S. Shi, and Y. Qi, "Review on modeling of the anode solid electrolyte interphase (SEI) for lithium-ion batteries," npj Comput. Mater. **4**, 15 (2018).

[10] J. K. Nørskov, J. Rossmeisl, A. Logadottir, L. Lindqvist, J. R. Kitchin, T. Bligaard, and H. Jonsson, "Origin of the overpotential for oxygen reduction at a fuel-cell cathode," J. Phys. Chem. B **108**, 17886–17892 (2004).

[11] J. K. Nørskov, T. Bligaard, A. Logadottir, J. Kitchin, J. G. Chen, S. Pandelov, and U. Stimming, "Trends in the exchange current for hydrogen evolution," J. Electrochem. Soc. **152**, J23 (2005).

[12] A. A. Peterson, F. Abild-Pedersen, F. Studt, J. Rossmeisl, and J. K. Nørskov, "How copper catalyzes the electroreduction of carbon dioxide into hydrocarbon fuels," Energy. Environ. Sci. **3**, 1311–1315 (2010).

[13] S. Ringe, N. G. Hormann, H. Oberhofer, and K. Reuter, "Implicit solvation methods for catalysis at electrified interfaces," Chem. Rev. **122**, 10777–10820 (2021).

[14] Z. Zhang and J. T. Yates, Jr., "Band bending in semiconductors: Chemical and physical consequences at surfaces and interfaces," Chem. Rev. **112**, 5520–5551 (2012).

[15] A. Klein, K. Albe, N. Bein, O. Clemens, K. A. Creutz, P. Erhart, M. Frericks, E. Ghorbani, J. P. Hofmann, B. Huang et al., "The Fermi energy as common parameter to describe charge compensation mechanisms: A path to Fermi level engineering of oxide electroceramics," J. Electroceram. **51**, 147 (2023).

[16] N. D. Mermin, "Thermal properties of the inhomogeneous electron gas," Phys. Rev. **137**, A1441 (1965).

[17] C. Bureau and G. Lécayon, "On a modeling of voltage-application to metallic electrodes using density functional theory," J. Chem. Phys. **106**, 8821–8829 (1997).

[18] U. Benedikt, W. B. Schneider, and A. A. Auer, "Modelling electrified interfaces in quantum chemistry: Constant charge vs. constant potential," Phys. Chem. Chem. Phys. **15**, 2712–2724 (2013).

[19] N. G. Hörmann, O. Andreussi, and N. Marzari, "Grand canonical simulations of electrochemical interfaces in implicit solvation models," J. Chem. Phys. **150**, 041730 (2019).

[20] N. G. Hörmann, N. Marzari, and K. Reuter, "Electrosorption at metal surfaces from first principles," npj Comput. Mater. **6**, 136 (2020).

[21] P. Lindgren, G. Kastlunger, and A. A. Peterson, "A challenge to the $g \sim 0$ interpretation of hydrogen evolution," ACS Catal. **10**, 121–128 (2020).

[22] A. Ge, G. Kastlunger, J. Meng, P. Lindgren, J. Song, Q. Liu, A. Zaslavsky, T. Lian, and A. A. Peterson, "On the coupling of electron transfer to proton transfer at electrified interfaces," J. Am. Chem. Soc. **142**, 11829–11834 (2020).

[23] N. G. Hörmann and K. Reuter, "Thermodynamic cyclic voltammograms: Peak positions and shapes," J. Phys.: Condens. Matter **33**, 264004 (2021).

[24] A. Kopač Lautar, A. Hagopian, and J.-S. Filhol, "Modeling interfacial electrochemistry: Concepts and tools," Phys. Chem. Chem. Phys. **22**, 10569–10580 (2020).

[25] N. Karmodak and O. Andreussi, "Catalytic activity and stability of two-dimensional materials for the hydrogen evolution reaction," ACS Energy Lett. **5**, 885–891 (2020).

[26] X. Chia and M. Pumera, "Characteristics and performance of two-dimensional materials for electrocatalysis," Nat. Catal. **1**, 909–921 (2018).

[27] S. Vijay, J. A. Gauthier, H. H. Heenen, V. J. Bukas, H. H. Kristoffersen, and K. Chan, "Dipole-field interactions determine the CO_2 reduction activity of 2D Fe–N–C single-atom catalysts," ACS Catal. **10**, 7826–7835 (2020).

[28] W. Ju, A. Bagger, N. R. Saharie, S. Möhle, J. Wang, F. Jaouen, J. Rossmeisl, and P. Strasser, "Electrochemical carbonyl reduction on single-site M–N–C catalysts," Commun. Chem. **6**, 212 (2023).

[29] N. Mounet, M. Gibertini, P. Schwaller, D. Campi, A. Merkys, A. Marrazzo, T. Sohier, I. E. Castelli, A. Cepellotti, G. Pizzi, and N. Marzari, "Two-dimensional materials from high-throughput computational exfoliation of experimentally known compounds," Nat. Nanotechnol. **13**, 246–252 (2018).

[30] S. Sun, Y. Qi, and T.-Y. Zhang, "Dissecting graphene capacitance in electrochemical cell," Electrochim. Acta **163**, 296–302 (2015).

[31] Y. Yu, K. Zhang, H. Parks, M. Babar, S. Carr, I. M. Craig, M. Van Winkle, A. Lyssenko, T. Taniguchi, K. Watanabe et al., "Tunable angle-dependent electrochemistry at twisted bilayer graphene with moiré flat bands," Nat. Chem. **14**, 267–273 (2022).

[32] Z. Wang, J. Chen, C. Ni, W. Nie, D. Li, N. Ta, D. Zhang, Y. Sun, F. Sun, Q. Li, Y. Li, R. Chen, T. Bu, F. Fan, and C. Li, "Visualizing the role of applied voltage in non-metal electrocatalysts," Natl. Sci. Rev. **10**, nwad166 (2023).

[33] J. Li and P. J. Burke, "Measurement of the combined quantum and electrochemical capacitance of a carbon nanotube," Nat. Commun. **10**, 3598 (2019).

[34] J. Li, P. H. Pham, W. Zhou, T. D. Pham, and P. J. Burke, "Carbon-nanotube–electrolyte interface: Quantum and electric double layer capacitance," ACS Nano **12**, 9763–9774 (2018).

[35] I. Heller, J. Kong, K. A. Williams, C. Dekker, and S. G. Lemay, "Electrochemistry at single-walled carbon nanotubes: The role of band structure and quantum capacitance," J. Am. Chem. Soc. **128**, 7353–7359 (2006).

[36] K. Schwarz and R. Sundararaman, "The electrochemical interface in first-principles calculations," Surf. Sci. Rep. **75**, 100492 (2020).

[37] P. Giannozzi, S. Baroni, N. Bonini, M. Calandra, R. Car, C. Cavazzoni, D. Ceresoli, G. L. Chiarotti, M. Cococcioni, I. Dabo et al., "QUANTUM ESPRESSO: A modular and open-source software project for quantum simulations of materials," J. Phys.: Condens. Matter **21**, 395502 (2009).

[38] P. Giannozzi, O. Andreussi, T. Brumme, O. Bunau, M. Buongiorno Nardelli, M. Calandra, R. Car, C. Cavazzoni, D. Ceresoli, M. Cococcioni et al., "Advanced capabilities for materials modelling with QUANTUM ESPRESSO," J. Phys.: Condens. Matter **29**, 465901 (2017).

[39] S. P. Huber, "Automated reproducible workflows and data provenance with AiiDA," Nat. Rev. Phys. **4**, 431 (2022).

[40] K. F. Garrity, J. W. Bennett, K. M. Rabe, and D. Vanderbilt, "Pseudopotentials for high-throughput DFT calculations," Comput. Mater. Sci. **81**, 446–452 (2014).

28 June 2024 08:41:02

[41] J. P. Perdew, K. Burke, and M. Ernzerhof, "Generalized gradient approximation made simple," Phys. Rev. Lett. **77**, 3865 (1996).

[42] P. Borlido, T. Aull, A. W. Huran, F. Tran, M. A. Marques, and S. Botti, "Large-scale benchmark of exchange–correlation functionals for the determination of electronic band gaps of solids," J. Chem. Theory Comput. **15**, 5069–5079 (2019).

[43] R. Sabatini, T. Gorni, and S. De Gironcoli, "Nonlocal van der Waals density functional made simple and efficient," Phys. Rev. B **87**, 041108 (2013).

[44] J. Heyd, G. E. Scuseria, and M. Ernzerhof, "Hybrid functionals based on a screened Coulomb potential," J. Chem. Phys. **118**, 8207–8215 (2003).

[45] O. Andreussi, I. Dabo, and N. Marzari, "Revised self-consistent continuum solvation in electronic-structure calculations," J. Chem. Phys. **136**, 064102 (2012).

[46] I. Dabo, B. Kozinsky, N. E. Singh-Miller, and N. Marzari, "Electrostatics in periodic boundary conditions and real-space corrections," Phys. Rev. B **77**, 115139 (2008).

[47] A. Curutchet, P. Colinet, C. Michel, S. N. Steinmann, and T. Le Bahers, "Two-sites are better than one: Revisiting the OER mechanism on CoOOH by DFT with electrode polarization," Phys. Chem. Chem. Phys. **22**, 7031–7038 (2020).

[48] M. M. Melander, T. Wu, T. Weckman, and K. Honkala, "Constant inner potential DFT for modelling electrochemical systems under constant potential and bias," npj Comput. Mater. **10**, 5 (2024).

[49] N. Abidi, K. R. G. Lim, Z. W. Seh, and S. N. Steinmann, "Atomistic modeling of electrocatalysis: Are we there yet?," WIREs Comput. Mol. Sci. **11**, e1499 (2021).

[50] T. Binninger, "Piecewise nonlinearity and capacitance in the joint density functional theory of extended interfaces," Phys. Rev. B **103**, L161403 (2021).

[51] N. Marzari, D. Vanderbilt, A. De Vita, and M. C. Payne, "Thermal contraction and disordering of the Al(110) surface," Phys. Rev. Lett. **82**, 3296–3299 (1999).

[52] B. G. Walker, C. Molteni, and N. Marzari, "*Ab initio* molecular dynamics of metal surfaces," J. Phys.: Condens. Matter **16**, S2575 (2004).

[53] J. J. Jorgensen and G. L. W. Hart, "Effectiveness of smearing and tetrahedron methods: Best practices in DFT codes," Modell. Simul. Mater. Sci. Eng. **29**, 065014 (2021).

[54] F. J. dos Santos and N. Marzari, "Fermi energy determination for advanced smearing techniques," Phys. Rev. B **107**, 195122 (2023).

[55] N. G. Hörmann, Z. Guo, F. Ambrosio, O. Andreussi, A. Pasquarello, and N. Marzari, "Absolute band alignment at semiconductor-water interfaces using explicit and implicit descriptions for liquid water," npj Comput. Mater. **5**, 100 (2019).

[56] J. Junquera, M. H. Cohen, and K. M. Rabe, "Nanoscale smoothing and the analysis of interfacial charge and dipolar densities," J. Phys.: Condens. Matter **19**, 213203 (2007).

[57] Z. Guo, F. Ambrosio, W. Chen, P. Gono, and A. Pasquarello, "Alignment of redox levels at semiconductor–water interfaces," Chem. Mater. **30**, 94–111 (2018).

[58] X. Wen, X.-T. Fan, X. Jin, and J. Cheng, "Band alignment of 2D material–water interfaces," J. Phys. Chem. C **127**, 4132–4143 (2023).

[59] P. Cendula, S. D. Tilley, S. Gimenez, J. Bisquert, M. Schmid, M. Grätzel, and J. O. Schumacher, "Calculation of the energy band diagram of a photoelectrochemical water splitting cell," J. Phys. Chem. C **118**, 29599–29607 (2014).

[60] N. Kharche, J. T. Muckerman, and M. S. Hybertsen, "First-principles approach to calculating energy level alignment at aqueous semiconductor interfaces," Phys. Rev. Lett. **113**, 176802 (2014).

[61] T. Binninger, "First-principles theory of electrochemical capacitance," Electrochim. Acta **444**, 142016 (2023).

[62] R. Sundararaman, K. Letchworth-Weaver, and K. A. Schwarz, "Improving accuracy of electrochemical capacitance and solvation energetics in first-principles calculations," J. Chem. Phys. **148**, 144105 (2018).

[63] K. Letchworth-Weaver and T. Arias, "Joint density functional theory of the electrode-electrolyte interface: Application to fixed electrode potentials, interfacial capacitances, and potentials of zero charge," Phys. Rev. B **86**, 075140 (2012).

[64] L. Li, Y.-P. Liu, J.-B. Le, and J. Cheng, "Unraveling molecular structures and ion effects of electric double layers at metal water interfaces," Cell Rep. Phys. Sci. **3**, 100759 (2022).

[65] M. D. Stoller, C. W. Magnuson, Y. Zhu, S. Murali, J. W. Suk, R. Piner, and R. S. Ruoff, "Interfacial capacitance of single layer graphene," Energy Environ. Sci. **4**, 4685–4689 (2011).

[66] J. A. Gauthier, C. F. Dickens, H. H. Heenen, S. Vijay, S. Ringe, and K. Chan, "Unified approach to implicit and explicit solvent simulations of electrochemical reaction energetics," J. Chem. Theory Comput. **15**, 6895–6906 (2019).

[67] S. D. Beinlich, N. G. Hörmann, and K. Reuter, "Field effects at protruding defect sites in electrocatalysis at metal electrodes?," ACS Catal. **12**, 6143–6148 (2022).

[68] F. Domínguez-Flores and M. M. Melander, "Approximating constant potential dft with canonical dft and electrostatic corrections," J. Chem. Phys. **158**, 144701 (2023).

28 June 2024 08:41:02